

Integrated Solution for Electric Vehicle and Foreign Object Detection in the Application of Dynamic Inductive Power Transfer

Shi, Wenli; Dong, Jianning; Soeiro, Thiago Batista; Bauer, P.

DOI

[10.1109/TVT.2021.3112278](https://doi.org/10.1109/TVT.2021.3112278)

Publication date

2021

Document Version

Accepted author manuscript

Published in

IEEE Transactions on Vehicular Technology

Citation (APA)

Shi, W., Dong, J., Soeiro, T. B., & Bauer, P. (2021). Integrated Solution for Electric Vehicle and Foreign Object Detection in the Application of Dynamic Inductive Power Transfer. *IEEE Transactions on Vehicular Technology*, 70(11), 11365 - 11377. <https://doi.org/10.1109/TVT.2021.3112278>

Important note

To cite this publication, please use the final published version (if applicable). Please check the document version above.

Copyright

Other than for strictly personal use, it is not permitted to download, forward or distribute the text or part of it, without the consent of the author(s) and/or copyright holder(s), unless the work is under an open content license such as Creative Commons.

Takedown policy

Please contact us and provide details if you believe this document breaches copyrights. We will remove access to the work immediately and investigate your claim.

Integrated Solution for Electric Vehicle and Foreign Object Detection in the Application of Dynamic Inductive Power Transfer

Wenli Shi, *Student Member, IEEE*, Jianning Dong, *Member, IEEE*,
Thiago Batista Soeiro, *Senior Member, IEEE*, and Pavol Bauer, *Senior Member, IEEE*

Abstract—One of the challenges with the dynamic inductive power transfer (DIPT) technique is the electric vehicle detection (EVD) that helps the DIPT system to control the power supply of the transmitter. The EVD method applying auxiliary coils is a promising candidate because the flat shape of the auxiliary coils is suitable for the compact design. However, the EVD may fail when the metallic foreign object (MFO) is present. Therefore, the desire emerges in the integration design of the EVD and foreign object detection (FOD). The FOD can ensure the reliability of the EVD as well as the highly efficient operation of the DIPT system without MFOs. In this context, this paper proposes an integrated solution to the EVD and FOD well suited for DIPT systems. The integrated solution utilizes both passive coil sets (PCSs) and active coil sets (ACSs). Additionally, a novel detection resonant circuit (DRC) is proposed to realize EVD and FOD using the same coil sets and to amplify the measurement sensitivity. The operation mechanisms, the detection coil sets architecture, the design of the proposed resonant circuits and the detection procedure are detailed. Finally, a printed circuit board based prototype is built to validate the integrated functionality of the EVD and FOD in a DIPT prototype processing 1 kW output. Experiments considering the practical DIPT application scenarios are conducted, and the proposed detection method is able to achieve advantageously high sensitivity and no blind zone.

Index Terms—dynamic inductive power transfer, resonant circuits, electric vehicle detection, foreign object detection.

I. INTRODUCTION

THE inductive power transfer (IPT) technique has been extensively researched as it makes contactless energy transfer possible [1]–[3]. Charging pads without physical contacts make the IPT system resistive to chemicals, water and dust. Because of that, the IPT system has been widely used in various applications with different power ratings, e.g., biomedical implants [4], factory automation [5] and electric vehicles (EVs) [6]–[14]. As a promising candidate of EVs charging method, IPT technology can realize tens of kW power transferred over the air gap [6]–[10]. In [7], an IPT setup is reported to transfer 50 kW with the efficiency of 95.5%.

Copyright (c) 2015 IEEE. Personal use of this material is permitted. However, permission to use this material for any other purposes must be obtained from the IEEE by sending a request to pubs-permissions@ieee.org.

This work has received funding from the Electronic Components and Systems for European Leadership Joint Undertaking under grant agreement No 876868. This Joint Undertaking receives support from the European Union's Horizon 2020 research and innovation programme and Germany, Slovakia, Netherlands, Spain, Italy.

Wenli Shi, Jianning Dong, Thiago Batista Soeiro and Pavol Bauer are with the DCE&S/EEMCS, Delft University of Technology, Delft 2624 CP, The Netherlands (e-mail: w.shi-3, j.dong-4, t.batistasoeiro, p.bauer@tudelft.nl).

The dynamic IPT (DIPT) system for EVs enables battery charging while driving on the road [15], [16]. This can be used to reduce the required battery size and/or to extend the driving range. In a typical DIPT system, transmitters (Tx) are usually segmented charging pads [10], [13], [17], [18] or elongated tracks [1], [9], [19], [20] embedded under the road surface. When segmented charging pads are deployed, if all Txs are turned on, those uncoupled with the Rx will give rise to unnecessary power losses as well as leakage magnetic field which may be hazardous to nearby human beings and animals [21], [22]. Therefore, the DIPT Tx should be turned ON/OFF depending on the position of the EV [23]–[32], which makes an EV detection (EVD) function necessary.

The EVD methods can be broadly classified into three categories. The first kind measures the variation of system performances for EVD, which requires no auxiliary devices [23], [24], [27]. As the mutual coupling increases as the EV approaches to the Tx, variations can be observed in the phase angle between the primary input current and voltage [24] and also in the amplitude of the primary winding current [23] for a detuned DIPT system. The cost of this method is that the increment of the reactive power leads to lower system efficiency. In [27], the induced voltage of one Tx led by the winding current of the adjacent Tx and Rx is used for EVD, which could fail when the mutual coupling between Txs is too low. The second kind of EVD methods rely on the image, magnetic field and coordinate information extracted from auxiliary equipments including camera [29], satellite [30], magnetic sensor [28] and infrared light sensor [31]. To derive the position of EVs from the extracted information, dedicated algorithms and wireless communications may be required. There might be delay in the detection signal transfer process and some of the auxiliary equipment is of high cost to be integrated into the DIPT system. This makes this method not an ideal candidate for the dynamic EV charging application.

The third kind of EVD method applies auxiliary coils [25], [26], [32]. To realize efficient traffic management, the induction loop detector has been applied to detect vehicles around the traffic light [32]. The detection coils are buried under the pavements to detect the self-inductance reduction caused by the metallic body of the vehicles. In [25], [26], auxiliary coils are deployed on both Tx and Rx sides. The auxiliary coil on the Rx side is constantly energized, so the auxiliary coils on the Tx side have an increasing induced

voltage as the EV approaches. By analysing the pattern the induced voltage changes in different Tx side auxiliary coils, the position and speed of EVs can be estimated. The flat shape of the auxiliary coils has advantages in the integration design, which is appealing to DIPT systems. To avoid the interference of the main field, the auxiliary coils are designed to be decoupled with the charging pads. It can be achieved by selecting an auxiliary coil topology of different polarity from the charging pad [26], or by deploying the auxiliary coil with a distance to the charging pad [25]. The latter method is not favourable because the distance between Tx pads should be limited to reduce the power pulsation in DIPT applications [33]. The former method is advantageous for a compact design, while the auxiliary coil size should be limited to eliminate the coupling led by its deformation. For Tx side auxiliary coils with a limited size, metallic foreign objects (MFOs) can considerably change their self-inductance and coupling with the Rx side auxiliary coils [34], [35], which may cause the failure of the EVD function. Therefore, the foreign object detection (FOD) becomes necessary to ensure the reliability of the EVD. Moreover, the FOD can also protect the DIPT system from low efficiency operation and potential hazards led by MFOs.

Numerous FOD solutions have been reported in the IPT charging applications. They are divided into two types. The first one detects MFOs by observing any variation on system parameters resulted from the MFOs, including the coil quality factor [36], resonance or cut-off frequency [37], [38], and system efficiency [39]. In [39], it is observed that the MFO can be detected if it can make the system efficiency change from the rated value to a certain degree. It is a simple solution to implement and cost effective, but this is only feasible in low power IPT systems. In high power applications such as the dynamic charging of EVs, the deviation of system parameters caused by small MFOs is often minimal and difficult to detect.

The second type of FOD method relies on auxiliary coil sets mounted on the Tx side, which can be either passive [40]–[43] or active [34]. Due to the changing magnetic field, the eddy current induced in the MFO will in turn change the voltage induced in the passive coil sets (PCS). To have the changing magnetic field, the Tx should be turned on for the detection, and a zero coupling between the PCS and the Tx should be realized to improve the FOD sensitivity. WiTricity developed an overlapped detection coil to measure the imbalanced voltage resulted from MFOs [43]. The circuit is balanced and the detection voltage is close to zero only when there are no MFOs. To avoid the blind zone at every intersection of the coils, different sets of detection coils should be interleaved. A non-overlapped coil based detection method is presented in [40], which uses two coil arrays configured perpendicularly to each other. This configuration measures induced voltage difference for the FOD. However, when a thin MFO is placed onto the centre of a Double-D (DD) charging pad [44], the PCS may become ineffective because the net flux linkage through the MFO is close to zero. The active coil sets (ACS) based method relies on the impedance variations resulted from MFOs. Usually a resonant circuit is required to amplify the impedance variation for improving the detection

sensitivity. In [34], a parallel capacitor is used because of the fast decaying characteristic of the input impedance of the parallel resonant tank away from the resonance. Multiple ACSs are required to cover the surface of a charging pad. However, any couplings among the ACSs can detune the resonant circuit. Therefore, to maintain high accuracy and sensitivity, coordinating switches are required to avoid the simultaneous operation of multiple ACSs, which is costly and complex.

Based on the literature study, the research topics of EVD and FOD are mostly discussed separately. Although the reported auxiliary coil arrays in [40] can realize FOD and EVD when the Tx and Rx are operating, this method is not suitable for DIPT applications where the Tx should not be energized before identifying the position of EVs. The operation of the EVD using auxiliary coils can be affected by the MFO. This makes the FOD essential to maintain the reliability of the EVD, while the research gap lying in the integrated design of the EVD and FOD has not been addressed in DIPT applications. Herein, in order to detect the EVs and MFOs effectively at low cost, this paper proposes and develops a new integrated detection method based on PCSs and ACSs. A core part of the proposed detection method is the detection resonant circuit (DRC) which improves the detection sensitivity and enable the ACSs to process the detection signals for both EVD and FOD. Compared with the existing literature, the proposed work achieves zero-blind-zone for FOD without any coordinating switches to control the ACSs, and realizes EVD using the same set of circuits. This paper analyses the detailed operation mechanism and validates the proposed concept in experiments. The main contributions of this paper are listed as follows:

- 1) A PCSs topology delivering high detection sensitivity and no blind zone for FOD.
- 2) A ACSs topology having zero internal coupling and no blind zone for FOD, and it is naturally decoupled from the Tx.
- 3) A DRC topology capable of amplifying the magnetic field variation caused by the intrusion of MFOs and EVs.
- 4) Integration design of EVD and FOD using the same auxiliary coil sets.

The rest of the paper is organized as follows. In Section II, the mechanisms of EVD and FOD are explained. The proposed method is compared with the state of the art to highlight the contribution. Based on the introduced operation mechanisms, the integrated detection solution is presented. In Section III, the operating procedure of the proposed detection system is detailed. Finally, PCB coils and DRC are adapted into a 1 kW IPT system to validate the performance of the proposed integrated functionality of EVD and FOD.

II. DETECTION PRINCIPLES USING AUXILIARY COIL SETS

A. EVD Using Auxiliary Coil Sets

To achieve EVD, auxiliary coil sets are deployed on both the Tx and Rx pads. As presented in Fig. 1, the EV source coil (EVSC) is deployed onto the Rx pad to constantly produce the high frequent magnetic field. The high frequent magnetic field

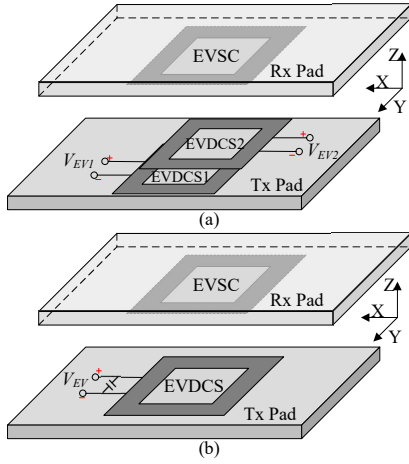


Fig. 1. EVD methods using auxiliary coil sets, (a) EVD method reported in [26], (b) proposed EVD method

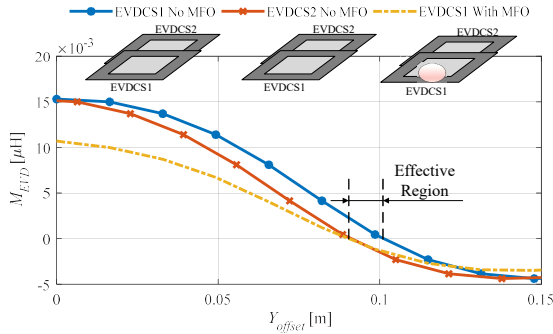


Fig. 2. Influence of MFOs on the reliability of the EVD method

is sensed by the EVD coil sets (EVDCS) applied onto the Tx pad. The phase and amplitude of the induced voltage in the EVDCS can be used to identify the position of the EV. The work in [26] proposed an EVD method detecting the phase of the induced voltage as shown in Fig. 1(a). This method applies two auxiliary coils (EVDCS1 and EVDCS2) onto the Tx pad with a spatial offset along the travelling direction. As shown in Fig. 2, the polarity of the mutual inductance M_{EVD} changes when the Rx pad approaches. Due to the spatial offset between the EVDCS1 and EVDCS2, there is an effective region where the polarities of their mutual inductance are opposite as highlighted in Fig. 2. By multiplying the induced voltages in EVDCS1 and EVDCS2 through an analog multiplier, the detection signal can be triggered when the Rx pad enters the effective region. However, the presence of MFO can lead to a change of M_{EVD} . As shown in Fig. 2, the effective region is minimal when the MFO is placed on EVDCS1 and the detection may fail.

In this paper, we propose an EVD method whose auxiliary coils can also be used for the FOD to ensure the reliability of the EVD. The proposed EVD method using the amplitude of the induced voltage in EVDCS. It is not practical to directly measure the induced voltage in EVDCS, because M_{EVD} is low and the current through the EVSC should be limited to reduce the power loss. As a result, the induced voltage in the EVDCS might be too low to be distinguishable. To solve

this problem, capacitors are applied to form a series resonant circuit with the EVDCS as shown in Fig. 1(b). The voltage across the capacitor V_{EV} can be expressed as

$$\begin{cases} V_{EV} = -jQ_{EVDCS}\omega_{EVD}M_{EVD}I_{EVSC} \\ Q_{EVDCS} = \frac{\omega_{EVD}L_{EVDCS}}{R_{EVDCS}} \end{cases} \quad (1)$$

where Q_{EVDCS} denotes the quality factor of the EVDCS, L_{EVDCS} and R_{EVDCS} are the self-inductance and resistance of the EVDCS, respectively. ω_{EVD} and I_{EVSC} are the angular switching frequency and current amplitude of the EVSC, respectively. It can be seen that V_{EV} is amplified by Q_{EVDCS} .

To ensure the reliability of the EVD, the interference from the main magnetic field and MFOs has to be addressed. Regarding the main magnetic field interference, the EVSC and EVDCS both should be decoupled from the charging pad, and the frequency of the EVSC current should be much higher than the rated charging frequency of 85 kHz, such that the induced voltage in EVDCS at 85 kHz can be attenuated by the DRC. When the MFO is placed on the EVDCS, its self-inductance drops [34] which could detune the DRC and the detection may fail. Therefore, it is essential to conduct FOD to ensure there is no MFO around the EVDCS.

B. FOD Using PCSs

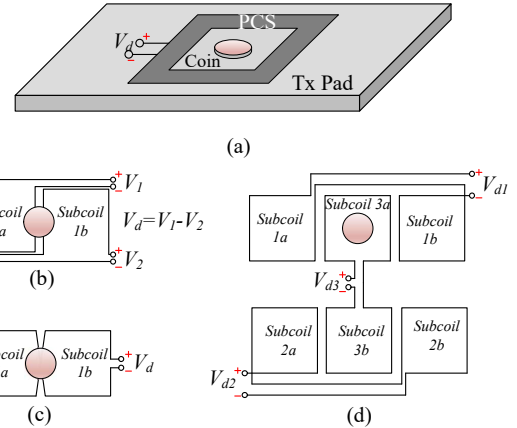


Fig. 3. FOD methods using PCSs, (a) the deployment of PCSs, (b) non-overlapped topology [40], (c) overlapped topology [43], (d) proposed topology

As illustrated in Fig. 3(a), the PCS is deployed onto the Tx pad to sense the variation of the magnetic field caused by MFOs. The variation of the magnetic field can be measured through the induced voltage of the PCSs. The FOD sensitivity S_{PCS} is expressed as

$$S_{PCS} = \left| \frac{\Delta V_d}{V_d} \right| \quad (2)$$

where V_d denotes the PCSs induced voltages, Δ represents the variation of a variable metric, e.g., voltage, caused by MFOs. To obtain high S_{PCS} to the MFO, one solution is to have V_d close to zero. Thus, it is necessary to keep the PCS decoupled from the Tx pad, which can be realized by

selecting a proper topology and position for the PCS. Another solution of increasing S_{PCS} is to enlarge ΔV_d , and it can be achieved by decreasing the size of the PCS [41]. However, ΔV_d is distinguishable when the MFO is placed within the area enclosed by the PCS. Thus, multiple small PCSs are applied to cover the area of the Tx pad [40]–[42].

It is reported that a PCS consists of two subcoils and the PCS behaves as a bipolar coil as shown in Fig. 3(b) [40] and 3(c) [43]. By locating the PCSs properly according to the feature of the main field, the total flux in each PCS can be minimal. Due to the symmetrical property of the PCSs in Fig. 3(b) and Fig. 3(c), the MFO symmetrically placed between two subcoils can hardly be detected and a blind zone emerges. To eliminate this blind zone, two layers of PCSs with a spatial offset are required [40], [43].

In this paper, one proposes a new PCS topology dedicated for DD charging pads as shown in Fig. 3(d). To eliminate the blind zone of the bipolar PCS, a subcoil of a unipolar PCS is deployed between the subcoils of the bipolar PCS, and it is not necessary to have another layer of PCSs. It should be mentioned that the unipolar and bipolar PCSs should be deployed according to the symmetric property of the DD pad to ensure they are decoupled.

C. FOD Using ACSs

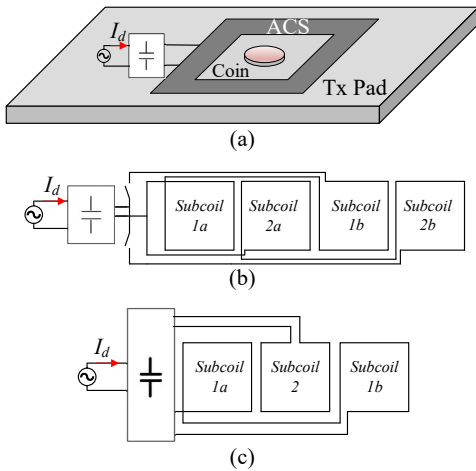


Fig. 4. FOD methods using ACSs, (a) topology in [34], (b) proposed topology.

The ACS depicted in Fig. 4(a) is powered by a dedicated AC source, and capacitors are applied to form the DRC. Instead of measuring the induced voltage like in the PCSs case, the input impedance Z_d is measured to identify the magnetic variation resulted from MFOs. When the MFO is coupled with the ACS, the self-inductance of the ACS L_{ACS} decreases [35]. ΔL_{ACS} can be measured through ΔZ_d . In the case that the MFO is of small size like coins, ΔL_{ACS} is minimal, while the corresponding ΔZ_d can be amplified by the DRC. The FOD sensitivity S_{ACS} is calculated as

$$S_{ACS} = \left| \frac{\Delta Z_d}{Z_d} \right| = G_r \left| \frac{\Delta L_{ACS}}{L_{ACS}} \right| \quad (3)$$

where G_r is the gain coefficient determined by the DRC. Since Z_d is measured by the input current I_d , the ACS is supposed to be decoupled with the Tx pad. To obtain high S_{ACS} , one approach is to design a DRC whose input impedance is sensitive to the resonance. Another approach is to decrease the size of the ACSs, such that the ratio of ΔL_{ACS} to L_{ACS} can be increased. However, if multiple ACSs are applied to cover the area of the Tx pad and operate at the same time, the coupling among ACSs will detune their DRC and switches should be applied [34] as shown in Fig. 4(b). In Fig. 4(b), a bipolar ACS is connected to a capacitor to form a parallel resonant circuit. To eliminate the blind zone, one subcoil of an ACS is placed between two subcoils of another ACS and switches are applied to avoid the simultaneous operation.

In this paper, one proposes a new ACS topology dedicated for DD charging pads as presented in Fig. 4(c). This topology includes both unipolar and bipolar ACSs. The unipolar coil is deployed between the subcoils of the bipolar coil. According to the field property, these two ACSs are internally decoupled which means no switches are required and the design of the DRC is simplified.

D. Integration of EVD and FOD

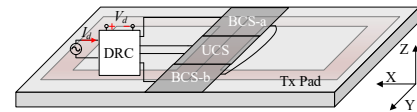


Fig. 5. Proposed auxiliary coil deployment over a DD charging pad.

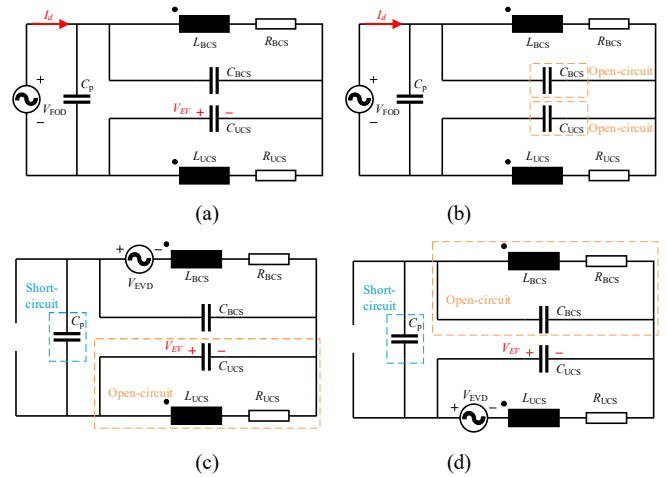


Fig. 6. Proposed DRC, (a) topology, (b) low frequency mode, (c) and (d) high frequency mode. V_{FOD} is the voltage source for FOD. V_{EVD} is the induced voltage in the auxiliary coil sets resulted from the coupling with the EVSC.

As discussed in Section II-A, the FOD should be conducted as an initializing step of the EVD. The FOD method using ACSs could be a good candidate because it can operate when the Tx is not energized. Then, the EVD and FOD rely on the DRC to amplify the magnetic field variation caused by the EVSC and MFO, respectively. This paper proposes an

integration design solution which can achieve EVD and FOD using the same auxiliary detection coil set. The integration design include the topology of the DRC and the deployment of the auxiliary coils, which are presented in Fig. 5 and Fig. 6.

In Fig. 5, three auxiliary coils are applied to form a unipolar coil set (UCS) and bipolar coil set (BCS) consisting of BCS-a and BCS-b. The UCS and BCS are placed along the ZY symmetric plane of the Tx pad. The advantage of the proposed coil deployment is that the UCS and BCS are both decoupled with the Tx. The interference of the main field on EVD and FOD can be eliminated. Meanwhile, the UCS and BCS are also decoupled from each other as depicted in Fig. 4(c). Thus, the UCS and BCS can be energized simultaneously as ACSs for FOD.

In Fig. 6, the proposed DRC adopts three capacitors (C_p , C_{BCS} and C_{UCS}) which are designed as follow

$$\begin{cases} \omega_{EVD} = 2\pi f_{EVD} \\ \omega_{FOD} = 2\pi f_{FOD} \\ C_{BCS} = \frac{1}{\omega_{EVD}^2 L_{BCS}} \\ C_{UCS} = \frac{1}{\omega_{EVD}^2 L_{UCS}} \\ C_p = \frac{1}{\omega_{FOD}^2 (L_{BCS} + L_{UCS})} \end{cases} \quad (4)$$

where L_{BCS} and L_{UCS} are the self-inductance of the BCS and UCS, respectively. When the operating frequency of the EVD f_{EVD} and FOD f_{FOD} satisfies $f_{FOD} \ll f_{EVD}$, the DRC can work in two different modes. When powered by the voltage source V_{FOD} , the DRC behaves in the low frequency mode as shown in Fig. 6(b). The parallel resonant tanks formed by L_{BCS} and C_{BCS} and by L_{UCS} and C_{UCS} have the input impedance $Z_{BCS,p}$ and $Z_{UCS,p}$. $Z_{BCS,p}$, $Z_{UCS,p}$ and the input impedance of the DRC Z_d can be calculated as

$$\begin{cases} Z_{BCS,p} = \frac{j\omega_{op}L_{BCS} + R_{BCS}}{j\omega_{op}C_{BCS}R_{BCS} + 1 - \omega_{op}^2 L_{BCS}C_{BCS}} \\ Z_{UCS,p} = \frac{j\omega_{op}L_{UCS} + R_{UCS}}{j\omega_{op}C_{UCS}R_{UCS} + 1 - \omega_{op}^2 L_{UCS}C_{UCS}} \\ Z_d = \frac{(Z_{BCS,p} + Z_{UCS,p})}{j\omega_{op}C_p(Z_{BCS,p} + Z_{UCS,p}) + 1} \end{cases} \quad (5)$$

where ω_{op} is the operating angular frequency. When $\omega_{op} = \omega_{FOD}$, $Z_{BCS,p}$ and $Z_{UCS,p}$ can be simplified as (6) according to the design requirements in (4). C_{UCS} and C_{BCS} can be seen as open-circuit. Thus, the DRC becomes a parallel resonant circuit comprised of C_p , L_{UCS} and L_{BCS} . When the DRC operates at f_{FOD} , its input impedance Z_d can be approximated as (7). The resistive part of Z_d is large due to the quality factor Q_{FOD} which can be as high as tens. Since Z_d is sensitive to the resonance [34], [45], Z_d will reduce significantly when there are MFOs as shown in Fig. 7. Thus, by measuring the increment of I_d , the MFO can be detected.

$$\begin{cases} Z_{BCS,p} \approx j\omega_{FOD}L_{BCS} + R_{BCS} \\ Z_{UCS,p} \approx j\omega_{FOD}L_{UCS} + R_{UCS} \end{cases} \quad (6)$$

$$\begin{cases} Z_d \approx (Q_{FOD} - j)\omega_{FOD}(L_{BCS} + L_{UCS}) \\ Q_{FOD} = \frac{\omega_{FOD}(L_{BCS} + L_{UCS})}{R_{BCS} + R_{UCS}} \end{cases} \quad (7)$$

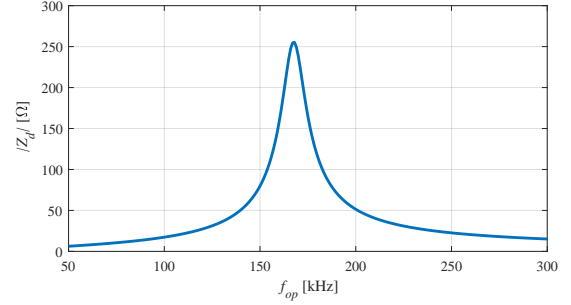


Fig. 7. Frequency response of Z_d , $\omega_{FOD} = 170\text{kHz}$.

When the EVSC is present, there will be the induced voltage V_{EVD} in the BCS and UCS and the DRC will operate in the high frequency mode as presented in Fig. 6(c) and 6(d). When $\omega_{op} = \omega_{EVD}$, $Z_{BCS,p}$ and $Z_{UCS,p}$ can be calculated as (8) based on (5). Due to the high coil quality factor Q_{EVD} , $Z_{BCS,p}$ and $Z_{UCS,p}$ are far larger than the reactance of C_{BCS} and C_{UCS} . When V_{EVD} is the input, the DRC behaves like a series resonant circuit consisting of L_{BCS} (L_{UCS}) and C_{BCS} (C_{UCS}). Thus, V_{EV} can be approximated as (9) where V_{EV} is Q_{EVD} times as high as V_{EVD} . By comparing the measured V_{EV} with a predefined value, the EVD can be realized.

$$\begin{cases} Z_{BCS,p} = (Q_{EVD} - j)\omega_{EVD}L_{BCS} \\ Z_{UCS,p} = (Q_{EVD} - j)\omega_{EVD}L_{UCS} \\ Q_{EVD} = \frac{\omega_{EVD}L_{BCS}}{R_{BCS}} = \frac{\omega_{EVD}L_{UCS}}{R_{UCS}} \end{cases} \quad (8)$$

$$\begin{cases} V_{EV} \approx jQ_{EVD}\omega_{EVD}I_{EVSC} \\ \quad \times (M_{EVD,BCS} + M_{EVD,UCS}) \end{cases} \quad (9)$$

E. Deployment of Auxiliary Coil Sets

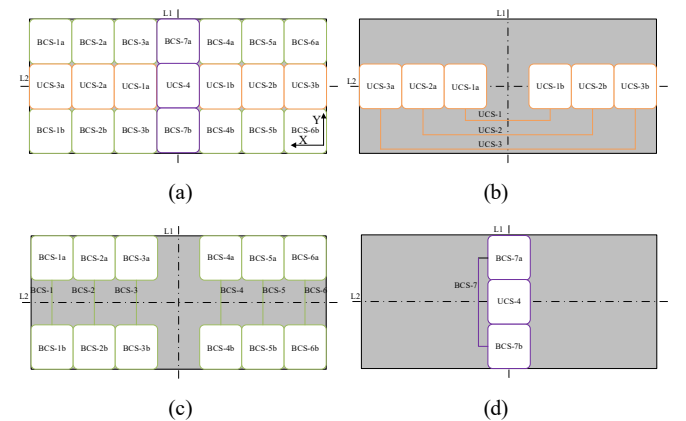


Fig. 8. Arrangement of auxiliary coil sets (a) overview, (b) and (c) PCSs, and (d) ACSs. L1 is the projection of the ZY symmetrical plane on the XY plane. L2 is the projection of the ZX symmetrical plane on the XY plane.

As the MFO may weaken the coupling between the Tx and the Rx pads and lead to extra eddy current losses, the FOD function should be effective over the area enclosed by the Tx pad. In Section II-D, the integration design of EVD and FOD is presented. However, to ensure a high FOD resolution, the size of ACSs should be limited [41] and only part of the Tx pad can be covered by the ACSs. To eliminate the FOD blind zone, PCSs are adopted to cover the rest of the area of the Tx. The coil arrangement is presented in Fig. 8.

Both the UCS and BCS are adopted for PCSs. The deployment of PCSs is illustrated in Fig. 8(b) and 8(c). UCS- i ($i = 1, 2$ and 3) consists of two rectangular coils, UCS-ia and UCS-ib, which are arranged symmetrically at L1 and connected in opposing series. BCS- i ($i=1, 2, \dots, 6$) is composed of two rectangular coils, BCS-ia and BCS-ib, placed symmetrically at L2 but connected in aiding series. According to the magnetic field property of the DD pad, the total flux in UCSs and BCSs is close to zero, which means they are decoupled with the Tx pad and high S_{PCS} can be guaranteed. Since the BCS can hardly detect the MFO placed on L2, a subcoil of the UCS is deployed in-between BCS-ia and BCS-ib. Thus, the blind zone over the area covered by PCSs is eliminated.

The deployment of ACSs are presented in Fig. 8(d), including UCS-4 and BCS-7. The EVSC is a UCS placed onto the Rx pad. Assuming that the EV travels along the Y axis, the coupling between the EVSC and ACSs are presented in Fig. 9. Based on (9), the range of V_{EV} can be calculated which can be used to define the threshold value for EVD.

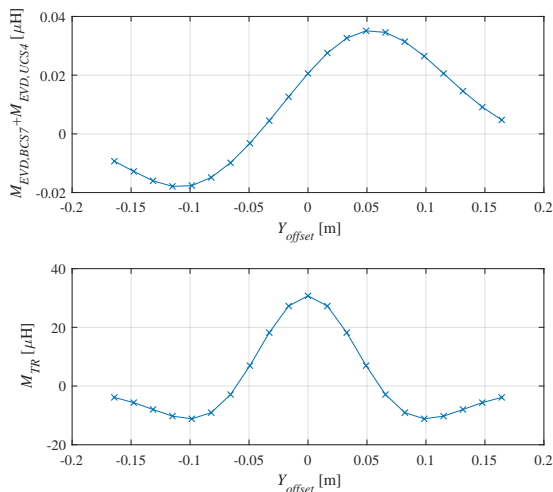


Fig. 9. Mutual coupling for EVD and the main coupling between the Tx and Rx M_{TR} computed by the finite element model.

III. DETECTION PROCEDURE

In the proposed DIPT system shown in Fig. 10, each Tx has five modules, FOD-ACS, FOD-PCS, EVD, power supply (PS) and Tx detection controller (TDC). The FOD-ACS module consists of a low voltage AC power supply at f_{FOD} , the DRC and the ACSs. This is used to detect MFOs over the ACSs illustrated in Fig. 8(d), and it operates before the Tx is energized. The FOD-PCS module consists of the PCSs requiring no power supply and it is used to detect MFOs in the

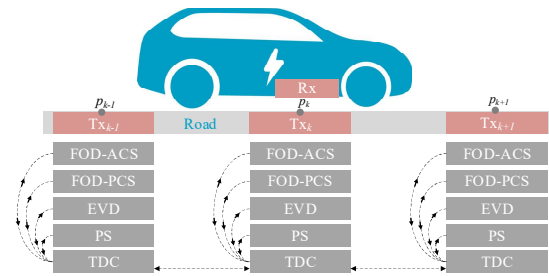


Fig. 10. DIPT systems applying the proposed detection method.

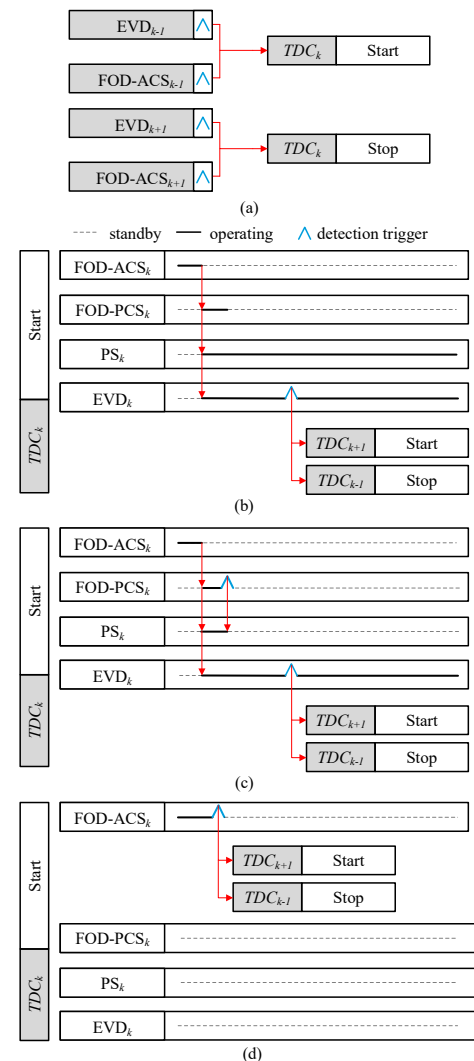


Fig. 11. Detection procedures, (a) communications among Tx_s and detection logics when there is (b) no MFOs, (c) a MFO on PCSs and (d) a MFO on ACSs.

area enclosed by the PCSs. The Tx pad has to be energized before the FOD-PCS module starts to detect MFOs. The EVD module consists of the DRC and the ACSs. The EVSC coil is mounted on the Rx side and powered by a low voltage AC power supply at f_{EVD} which is constantly on. It is used to identify whether there is an EV aligned with the Tx. The PS module is the power source of the Tx pad. As shown in Fig. 10 the TDC module is used to receive the detection

signals to control the operating sequence of each module and to communicate with the TDC module of adjacent Tx pads. It can enable and disable the FOD-ACS, FOD-PCS and EVD modules and process the detection results to determine the action of the PS module of the Tx. Thus, the PS can be switched on only when there are no MFOs and an EV is in the near range.

Due to the presence of resonant circuits in the Tx side, it takes some time for the winding current of the Tx pad to reach the rated value from its initial condition. To make full use of the limited effective charging zone of each Tx pad, it is practical to initialize and to start the Tx pad before the EV enters the effective charging zone. Therefore, T_{X_k} is designed to be started by the detection signal of $T_{X_{k-1}}$ and to be stopped by the detection signal of $T_{X_{k+1}}$ as shown in Fig. 11(a). The detailed detection logic is illustrated in Fig. 11(b), 11(c) and 11(d):

- Fig. 11(b), the detection trigger from $T_{X_{k-1}}$ enables the FOD-ACS module. The FOD-ACS module finds no MFOs and disable itself. Meanwhile, the FOD-PCS module, PS module and EVD module are enabled. The FOD-PCS module finds no MFOs and disables itself. The PS module stays in operation mode until the detection trigger is received from $T_{X_{k+1}}$. When the EV is aligned with T_{X_k} , a detection trigger is sent to stop $T_{X_{k-1}}$ and start $T_{X_{k+1}}$.
- Fig. 11(c), the detection trigger from $T_{X_{k-1}}$ enables the FOD-ACS module. The FOD-ACS module finds no MFOs and disables itself. Meanwhile, the FOD-PCS module, PS module and EVD module are enabled. The FOD-PCS module finds a MFO and disable itself and the PS module. When the EV is aligned with T_{X_k} , a detection trigger is sent to stop $T_{X_{k-1}}$ and start $T_{X_{k+1}}$.
- Fig. 11(d), the detection trigger from $T_{X_{k-1}}$ enables the FOD-ACS module. The FOD-ACS module finds a MFO and disables itself. Meanwhile, a detection trigger is sent to stop $T_{X_{k-1}}$ and start $T_{X_{k+1}}$.

IV. EXPERIMENTAL VALIDATION

In order to verify the proposed detection method, an IPT system is built as shown in Fig. 12. The Tx and Rx pads using DD coil topology are identical. The IPT system is compensated with double-sided LCC compensation tuned at 85 kHz. The IPT system circuit parameters are listed in Table I. Other details of the IPT system components are presented in Table II.

A. Design of Auxiliary coils and DRC

As shown in Fig. 8, the deployment of auxiliary detection coils is determined by the axis of symmetry of the Tx pads, L1 and L2. To guarantee the geometrical features of the auxiliary detection coils, the PCB coils are designed as shown in Fig. 13 and Fig. 14. On the Tx side, there are twenty-one identical auxiliary detection coils. Each auxiliary detection coil has ten number of turns with a length and width of 42.6 mm*54.7 mm. On the Rx side, EVSC coil consists of one single coil having five turns with a length and width of 298 mm*164

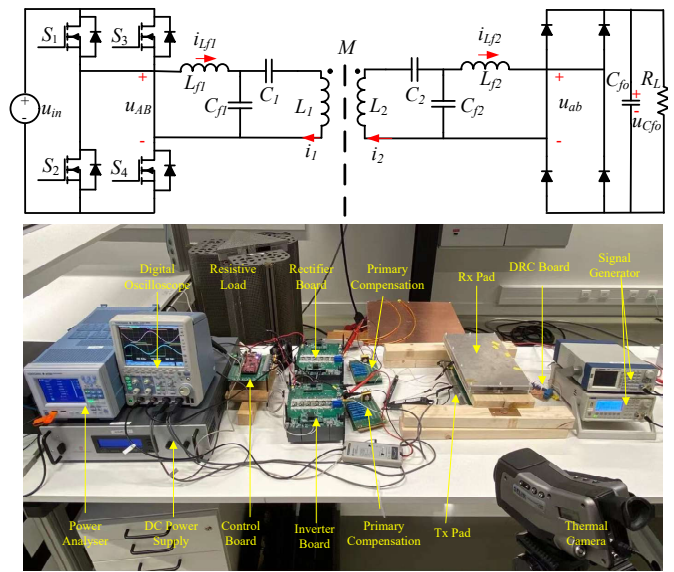


Fig. 12. IPT charging system using double-sided LCC compensation and DD Tx and Rx coils.

TABLE I
IPT SYSTEM CIRCUIT SPECIFICATIONS

Part	Unit	Value
L_1	μH	200.7
L_2	μH	203.5
M	μH	30
L_{f1}	μH	66.39
L_{f2}	μH	68.97
C_1	nF	26.87
C_2	nF	28.98
C_{f1}	nF	54.83
C_{f2}	nF	51.67
C_{fo}	μF	110
R_L	Ω	123

TABLE II
COMPONENT SPECIFICATIONS OF THE IPT SYSTEM

Part	Property
Ferrite	Material type: P, number of bars: 3, length of bars: 220 mm
Litz wire	Type: AWG 41, number of strands: 525
Coil	Topology: DD-DD, number of turns: 30, size: 172*298 mm ²
Capacitor	Polypropylene film, 6.7 nF
MOSFET	IMZ120R030MIH

mm. By using the impedance analyser (Agilent 4294A, 40 Hz to 110 MHz), the self-inductance and AC resistance R_{ac} of UCS-4 and BCS-7 are measured as listed in Table III.

In practice, it is hard to ensure that the auxiliary detection coils are strictly decoupled to the charging pads. The deflection and displacement of the PCB coil may lead to a certain coupling with the Tx pad. Therefore, it is essential to keep f_{PS} much smaller than f_{FOD} and avoid odd order harmonics of the PS such that the harmonics at f_{PS} can be bypassed. To test the performance of the PCB coil, f_{FOD} is selected to be around 170 kHz. The EVD frequency is selected to be around 1 MHz which satisfies $f_{FOD} \ll f_{EVD}$. The capacitors in the DRC are designed to be 200 nF for C_p , 4.3 nF for C_{UCS4} and 2.2 nF for C_{BCS7} .

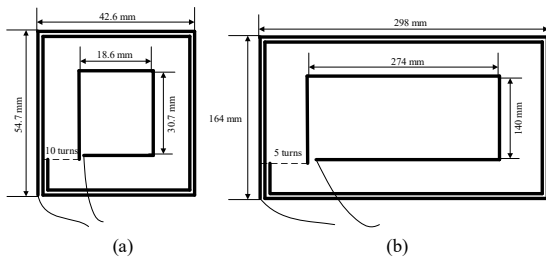


Fig. 13. Dimension of (a) a single auxiliary detection coil, (b) EVSC.

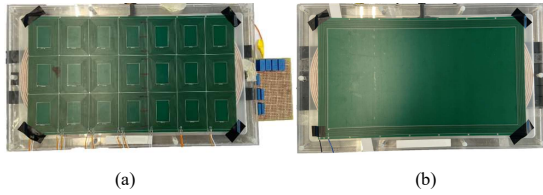


Fig. 14. PCB coils integrated to the charging pads, (a) Tx pad, (b) Rx pad.

TABLE III
COMPONENT SPECIFICATIONS OF THE IPT SYSTEM

Coil set	L [μH]	R_{ac} [$\text{m}\Omega$]
UCS-4	6.05	470
BCS-7	11.63	889
EVSC	15.4	360

B. FOD Function Using ACSs

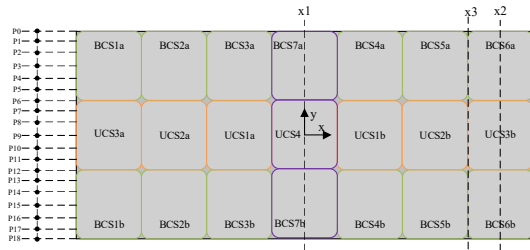


Fig. 15. MFO locations for the FOD test. Trajectory x1 for FOD-ACS. Trajectories x2 and x3 for FOD-PCS. Under each trajectory nineteen points are highlighted.

To verify the performance of FOD using the ACSs, an oneuro coin with diameter of 23.25 mm and thickness of 2.33 mm is taken as the reference MFO. According to the detection procedure in Fig. 11, the FOD-ACS module operates when the Rx pad is absent and the PS is off. A signal generator is applied to feed the ac power at f_{FOD} . The ACSs, including BCS-7 and UCS-4, are used to build the DRC together with the capacitors C_p , C_{BCS7} and C_{UCS4} . By measuring the input voltage V_{FOD} and current I_d , the input impedance Z_d variation caused by the MFO is obtained. The MFO moves along the trajectory x1 as shown in Fig. 15.

As shown in Fig. 16(a), the waveforms of V_{FOD} and I_d are in-phase, indicating a resistive Z_d around 205.1 Ω . A high input impedance helps to reduce the power loss in the ACSs. Due to the intrusion of the MFO at (x1,P4) in Fig. 16(b), Z_d drops to 158.8 Ω , indicating a 22.6% reduction of Z_d . This is

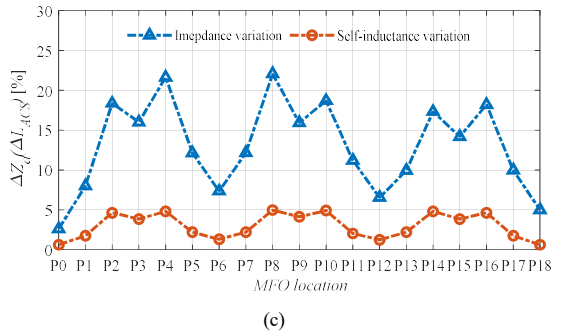
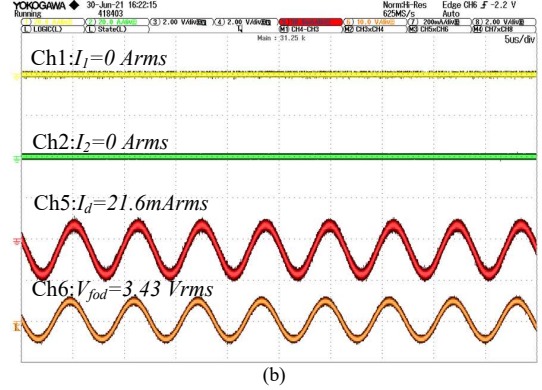
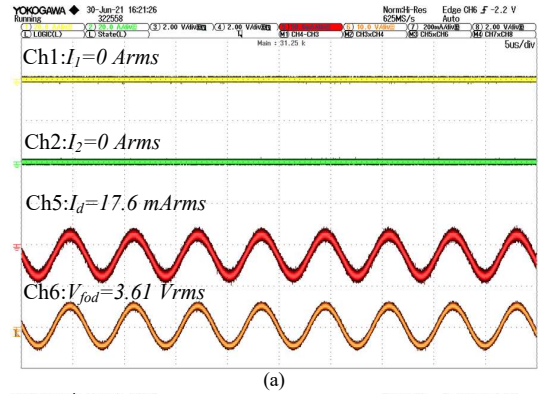


Fig. 16. Experimental results of FOD using ACS. Waveforms of V_{FOD} and I_d (a) with no MFOs, and (b) with the MFO at (x1, P4), and (c) full-range performance when the MFO moves along trajectory x1.

a consequence of a 3.9% reduction of the total self-inductance of the ACSs L_{ACS} .

Fig. 16(c) presents the full-range FOD performance of the ACSs. Compared with the curve of ΔL_{ACS} , ΔZ_d shows the same trend and an obvious positive scaling factor. It can be seen that ΔL_{ACS} becomes relatively high when the MFO is placed near the centre of the ACSs, while the peaks are not at center points P3, P9 and P15. According to [35], the self-inductance reduction of the ACS ΔL_{ACS} is determined by its coupling with the MFO as

$$\Delta L_{ACS} = \frac{\omega_{FOD}^2 M_{MFO,A}^2 L_{MFO}}{\omega_{FOD}^2 L_{MFO}^2 + R_{MFO}^2} \quad (10)$$

where L_{MFO} , $M_{MFO,A}$ and R_{MFO} are the equivalent self-inductance, mutual inductance with the ACSs and resistance of the MFO, respectively. As illustrated in Fig. 17, the magnetic field becomes stronger at points close to the inner edges of

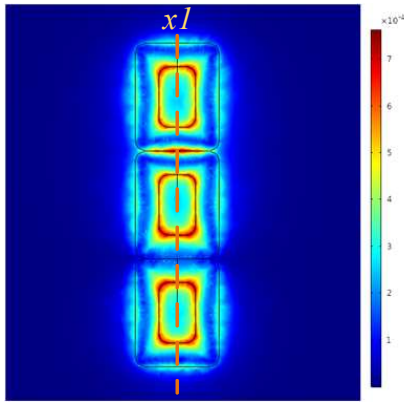


Fig. 17. Magnetic field distribution (unit T) when 1 A current is applied to the ACSs.

the ACSs. Thus, $M_{MFO,A}$ at points P2 and P4 is higher than that at point P3. Based on (10), ΔL_{ACS} at points P2 and P4 is also higher than that at point P3. The same reason can be applied to explain the dips at points P9 and P15. According to Fig. 7, ΔZ_d increases as the resonant frequency of the DRC deviates away from f_{FOD} . Therefore, ΔZ_d has the same trend as ΔL_{ACS} . The maximum ΔL_{ACS} is around 5% with the MFO at P2, P4, P8, P10, P14 and P16 and the corresponding ΔZ_d is higher than 17%. The influence of the MFO becomes weaker as it approaches to the outer edge of the ACSs. The minimum ΔL_{ACS} is around 0.63% with the MFO at P0 and P18, while the corresponding ΔZ_d is about four times higher, around 2.6%. In summary, by virtue of the proposed DRC, the influence of the MFO on the ACSs is considerably amplified. The FOD of high sensitivity and no blind zone is achieved within the area enclosed by the ACSs.

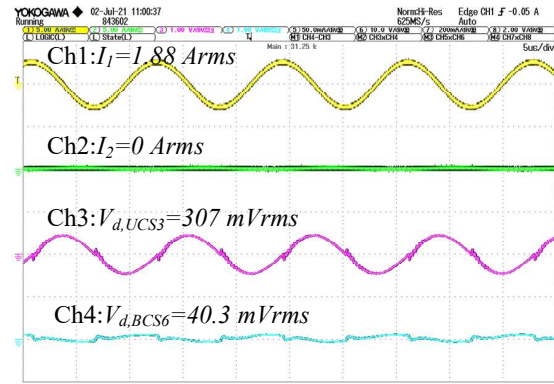
C. FOD Function Using PCSs

According to the detection procedure in Fig. 11, the FOD-PCS module operates when the Rx pad is absent and the PS is on. The Tx pad is powered by a winding current I_1 of 1.88 Arms. With the intrusion of the MFO an increment of the induced voltage V_d can be observed from the studied PCSs, UCS-3 and BCS-6. The MFO moves along the trajectory x2 and x3 as shown in Fig. 15.

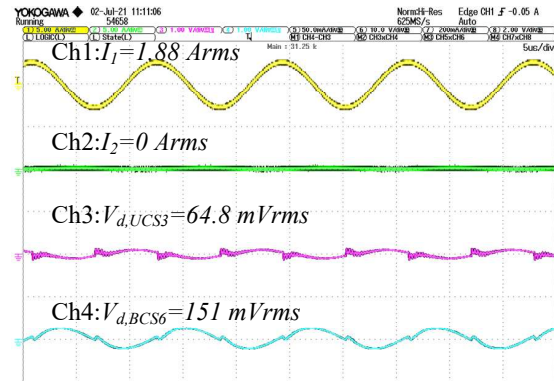
Fig. 18(a) and 18(b) present the waveforms of V_d when the MFO is placed at (x2, P8) and (x2, P2), where $V_{d,UCS3}$ and $V_{d,BCS6}$ are the measured induced voltage of UCS-3 and BCS-6, respectively. Fig. 18(c) shows the full-range FOD performance of the PCSs. The value of V_d is determined by the coupling of the MFO with the PCSs and the main field distribution. Based on (10), the self-inductance reduction of the PCS ΔL_{PCS} can reflect its coupling with the MFO $M_{MFO,P}$ as

$$M_{MFO,P} = \frac{1}{\omega_{PS}} \sqrt{\frac{(\omega_{PS}^2 L_{MFO}^2 + R_{MFO}^2) \Delta L_{PCS}}{L_{MFO}}} \quad (11)$$

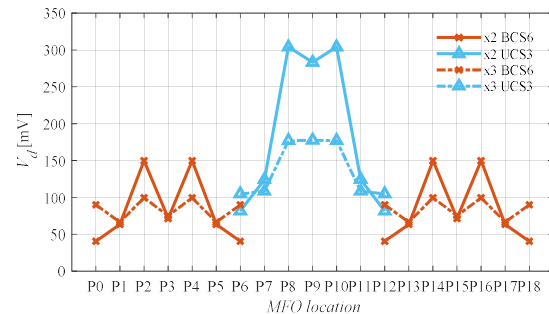
where ω_{PS} is the angular frequency of the PS. Based on (11), Fig. 19(a) can prove that $M_{MFO,P}$ at trajectory x2 is



(a)



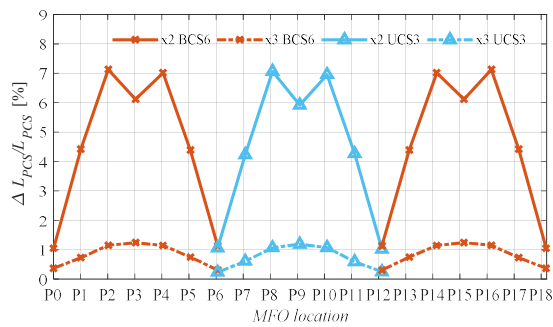
(b)



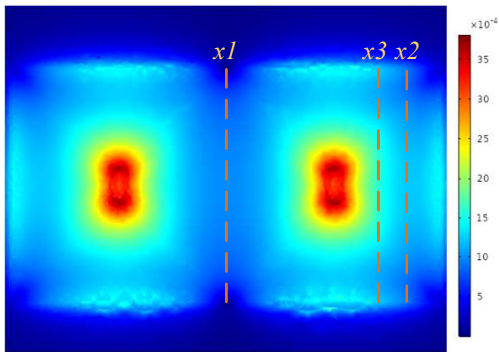
(c)

Fig. 18. Experimental results of FOD using PCS. Waveforms of V_d with the MFO (a) at (x2, P8) and (b) at (x2, P2), and (c) full-range performance when the MFO moves along trajectory x2 and x3.

consistently higher than that at trajectory x3. However, the magnetic field at trajectory x3 is stronger than that at trajectory x2 as depicted in Fig. 19(b). As shown in Fig. 19(a), $M_{MFO,P}$ at (x2, P8) is close to that at (x2, P2), while the magnetic field is higher at (x2, P8). As a result, V_d at (x2, P8) has a larger value than that at (x2, P2). Due to the magnetic field distribution, V_d of trajectory x2 is lower than that of trajectory x3 at points P0, P6, P12, and P18 although $M_{MFO,P}$ of trajectory x2 is slightly higher. At other points, $M_{MFO,P}$ of trajectory x2 are significantly higher than that of trajectory x3. As a consequence, V_d of trajectory x2 is higher than or close to that of trajectory x3 at these points. In summary, the proposed design of the PCSs can effectively identify MFOs within the area enclosed by the PCSs.



(a)



(b)

Fig. 19. Finite element model results, (a) the normalized self-inductance reduction of PCSs led by MFOs, (b) the magnetic field distribution (unit T).

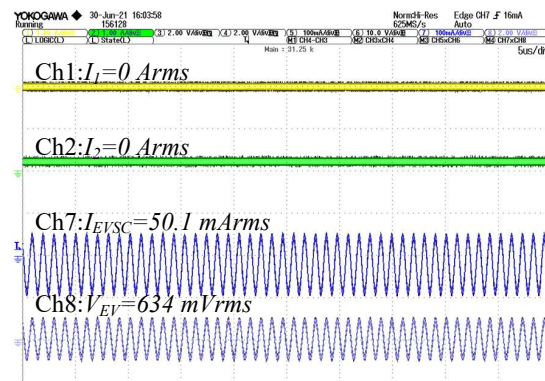
D. EVD Function Using ACSs

To validate the performance of the EVD using ACSs, the EVSC is powered by a signal generator at f_{EVD} and the ACSs are used to sense their coupling with the EVSC. The coupling between the ACSs and the EVSC increases when the Rx pad approaches to the Tx pad. The induced voltage in the ACSs can be amplified in V_{EV} by the DRC. Thus, by comparing with a predefined threshold voltage, the alignment condition of the Rx pad can be identified and the EVD can be accomplished with a high sensitivity.

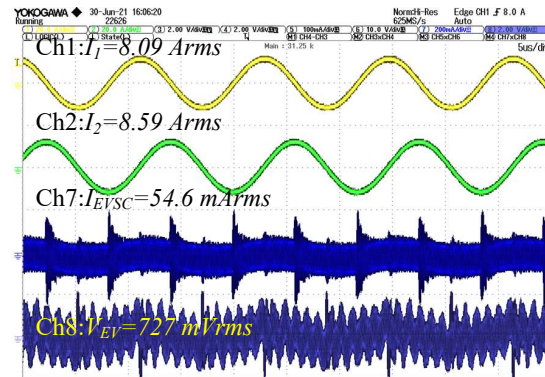
According to the detection procedure in Fig. 11, the EVD module operates when there is no MFO on the ACSs and the PS can be either on or off. Fig. 20 presents the waveform of V_{EV} and I_{EVSC} when the Rx pad is aligned with the Tx pad. When the PS is off, the rms value of V_{EV} is 634 mV with I_{EVSC} equal to 50.1 mA, as shown in Fig. 20(a). In Fig. 20(b) the PS is on, and the rms value of V_{EV} slightly increases to 727 mV. It is because the EVSC is relative large and not perfectly decoupled with the Rx pad, and the 85 kHz harmonics emerges in the waveform of I_{EVSC} and V_{EV} . The harmonics can be filtered, since the frequency of the harmonics is much smaller than f_{EVD} . In summary, the DRC formed by the ACSs can effectively identify the alignment condition of the EV by measuring the rms value of V_{EV} .

E. System Performances in Practical Scenarios

To investigate the influence of the detection modules on the power transfer, the dc-dc efficiency of the system is measured at 1 kW output power when the Rx is aligned with the Tx as illustrated in Fig. 21. Due to the presence of the PCB



(a)



(b)

Fig. 20. Measured waveform of V_{EV} , I_{EVSC} and I_d when the Tx and Rx are aligned, with (a) PS off and (b) PS on.

coils together with the DRC, the measured efficiency drops by 0.48%, which is minimal. Considering that the power analyser (YOKOGAMA WT500) has a basic measurement uncertainty about 0.1% of the reading plus 0.1% of the range, the efficiency difference led by the PCB coils is comparable with the measurement uncertainty.

To verify the performance of the proposed detection method, experiments are conducted considering the DIPT application scenarios as depicted in Fig. 22. It is assumed that the distance between two Tx pads is 28 cm. According to the detection procedures in Fig. 11, the FOD-ACS module is enabled when the Rx reaches p_{k-1} as shown in Fig. 23(a) and 23(d). If there is no MFO on the ACSs, the FOD-PCS module and PS module will be enabled as presented in Fig. 23(b) and 23(e). When the Rx reaches p_k and FOD-ACS module is not triggered, the EVD will be triggered as per Fig. 23(c) and 23(f).

In the comparison between Fig. 23(a) and 23(d), the input impedance Z_d changed by around 20% which proves the effectiveness of the FOD-ACS module. It should be mentioned that V_{EV} has harmonics at f_{FOD} because V_{FOD} is shared by L_{BCS7} and L_{UCS4} according to the DRC in Fig. 6(b). This does not affect the operation of EVD module because EVD module is enabled after the operation of FOD-ACS module.

In the comparison between Fig. 23(b) and 23(e), $V_{d,UCS3}$ changes from 186 mVrms to 1103 mVrms due to the MFO placed on UCS-3. The change in $V_{d,BCS6}$ is insignificant although the MFO is close to BCS-6. In Fig. 23(c) and 23(f) both Rx and Tx are energized so the magnetic field is stronger

than that in Fig. 23(b) and 23(e). Correspondingly, $V_{d,UCS3}$ and $V_{d,BCS6}$ increase slightly. To avoid the fault detection of the FOD-PCS module, the predefined threshold value should be selected based on the measurements in Fig. 23(c) and 23(e). Taking UCS-3 as an example, $V_{d,UCS3}$ is 381 mVrms in Fig. 23(c) and 1103 mVrms in Fig. 23(e). Thus, the threshold value should be between these two measured value.

As the Rx moves from p_{k-1} to p_k , the mutual coupling between the EVSC and ACSs increases as shown in Fig. 9. Therefore, V_{EV} increases from 405 mVrms in Fig. 23(b) to 752 mVrms in Fig. 23(c), which proves that the main field does not affect the effectiveness of the EVD module. Besides, it is also proved by Fig. 23(f) that the presence of the MFO on PCSs has no influence on the operation of the EVD module.

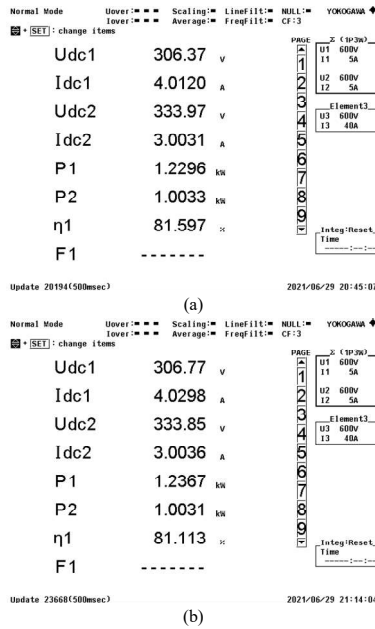


Fig. 21. System efficiency at 1 kW output power (a) with no PCB coils and (b) with PCB coils connected to the DRC.

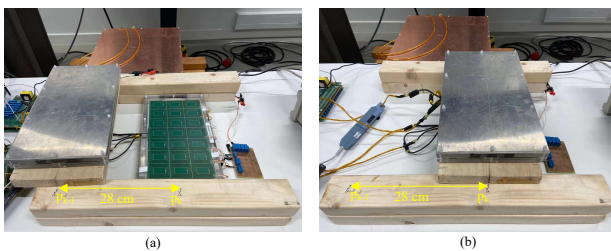


Fig. 22. Experiments considering the real practical scenarios. The Rx is (a) aligned with Tx_{k-1} at p_{k-1} and (b) aligned with Tx_k at p_k . The distance between p_{k-1} and p_k is 28 cm.

V. CONCLUSION

This paper proposes an integrated detection method that applies the same auxiliary detection coil sets to realize both EVD and FOD for DIPT systems. The proposed detection system mainly consists of auxiliary detection coil sets and a DRC. Different from the existing topology of auxiliary coil

sets, the proposed detection coil sets apply both PCSs and ACSs to eliminate the blind zone and gain a high sensitivity to the intrusion of MFOs. Beside, a DRC topology is proposed to further amplify the influence of MFOs and EVs on auxiliary detection coil sets to make EVD and FOD more effective and reliable. Aiming at DIPT applications, the detection procedures are introduced and the operating conditions of the detection modules are concluded. The proposed design mainly includes the FOD-ACS module, the FOD-PCS module and the EVD module. To validate the proposed detection method, PCB coils are designed and integrated into an IPT system. According to the operating conditions of the detection modules, experiments are conducted for each detection modules as well as the entire system considering the practical DIPT application scenarios. Based on the experimental results, the proposed design is able to realize reliable EVD and FOD functions with high sensitivity and no blind zone.

REFERENCES

- [1] C. C. Mi, G. Buja, S. Y. Choi, and C. T. Rim, "Modern Advances in Wireless Power Transfer Systems for Roadway Powered Electric Vehicles," *IEEE Transactions on Industrial Electronics*, vol. 63, no. 10, pp. 6533–6545, Oct. 2016.
- [2] G. A. Covic and J. T. Boys, "Inductive Power Transfer," *Proceedings of the IEEE*, vol. 101, no. 6, pp. 1276–1289, Jun. 2013.
- [3] S. Y. Choi, B. W. Gu, S. Y. Jeong, and C. T. Rim, "Advances in Wireless Power Transfer Systems for Roadway-Powered Electric Vehicles," *IEEE Journal of Emerging and Selected Topics in Power Electronics*, vol. 3, no. 1, pp. 18–36, Mar. 2015.
- [4] P. Si, A. P. Hu, S. Malpas, and D. Budgett, "A Frequency Control Method for Regulating Wireless Power to Implantable Devices," *IEEE Transactions on Biomedical Circuits and Systems*, vol. 2, no. 1, pp. 22–29, Mar. 2008.
- [5] J. T. Boys, G. A. Covic, and A. W. Green, "Stability and control of inductively coupled power transfer systems," *IEE Proceedings - Electric Power Applications*, vol. 147, no. 1, pp. 37–43, Jan. 2000.
- [6] S. Kim, G. A. Covic, and J. T. Boys, "Comparison of Tripolar and Circular Pads for IPT Charging Systems," *IEEE Transactions on Power Electronics*, vol. 33, no. 7, pp. 6093–6103, Jul. 2018.
- [7] R. Bosshard, U. Iruretagoyena, and J. W. Kolar, "Comprehensive Evaluation of Rectangular and Double-D Coil Geometry for 50 kW/85 kHz IPT System," *IEEE Journal of Emerging and Selected Topics in Power Electronics*, vol. 4, no. 4, pp. 1406–1415, Dec. 2016.
- [8] G. R. Nagendra, G. A. Covic, and J. T. Boys, "Determining the Physical Size of Inductive Couplers for IPT EV Systems," *IEEE Journal of Emerging and Selected Topics in Power Electronics*, vol. 2, no. 3, pp. 571–583, Sep. 2014.
- [9] S. Y. Choi, S. Y. Jeong, B. W. Gu, G. C. Lim, and C. T. Rim, "Ultraslim S-Type Power Supply Rails for Roadway-Powered Electric Vehicles," *IEEE Transactions on Power Electronics*, vol. 30, no. 11, pp. 6456–6468, Nov. 2015.
- [10] G. R. Nagendra, G. A. Covic, and J. T. Boys, "Sizing of Inductive Power Pads for Dynamic Charging of EVs on IPT Highways," *IEEE Transactions on Transportation Electrification*, vol. 3, no. 2, pp. 405–417, Jun. 2017.
- [11] W. Zhang and C. C. Mi, "Compensation Topologies of High-Power Wireless Power Transfer Systems," *IEEE Transactions on Vehicular Technology*, vol. 65, no. 6, pp. 4768–4778, Jun. 2016.
- [12] U. K. Madawala and D. J. Thrimawithana, "A Bidirectional Inductive Power Interface for Electric Vehicles in V2G Systems," *IEEE Transactions on Industrial Electronics*, vol. 58, no. 10, pp. 4789–4796, Oct. 2011.
- [13] S. Cui, Z. Wang, S. Han, C. Zhu, and C. C. Chan, "Analysis and Design of Multiphase Receiver with Reduction of Output Fluctuation for EV Dynamic Wireless Charging System," *IEEE Transactions on Power Electronics*, pp. 1–1, 2018.
- [14] L. Zhao, D. J. Thrimawithana, U. K. Madawala, A. P. Hu, and C. C. Mi, "A Misalignment-Tolerant Series-Hybrid Wireless EV Charging System With Integrated Magnetics," *IEEE Transactions on Power Electronics*, vol. 34, no. 2, pp. 1276–1285, Feb. 2019.

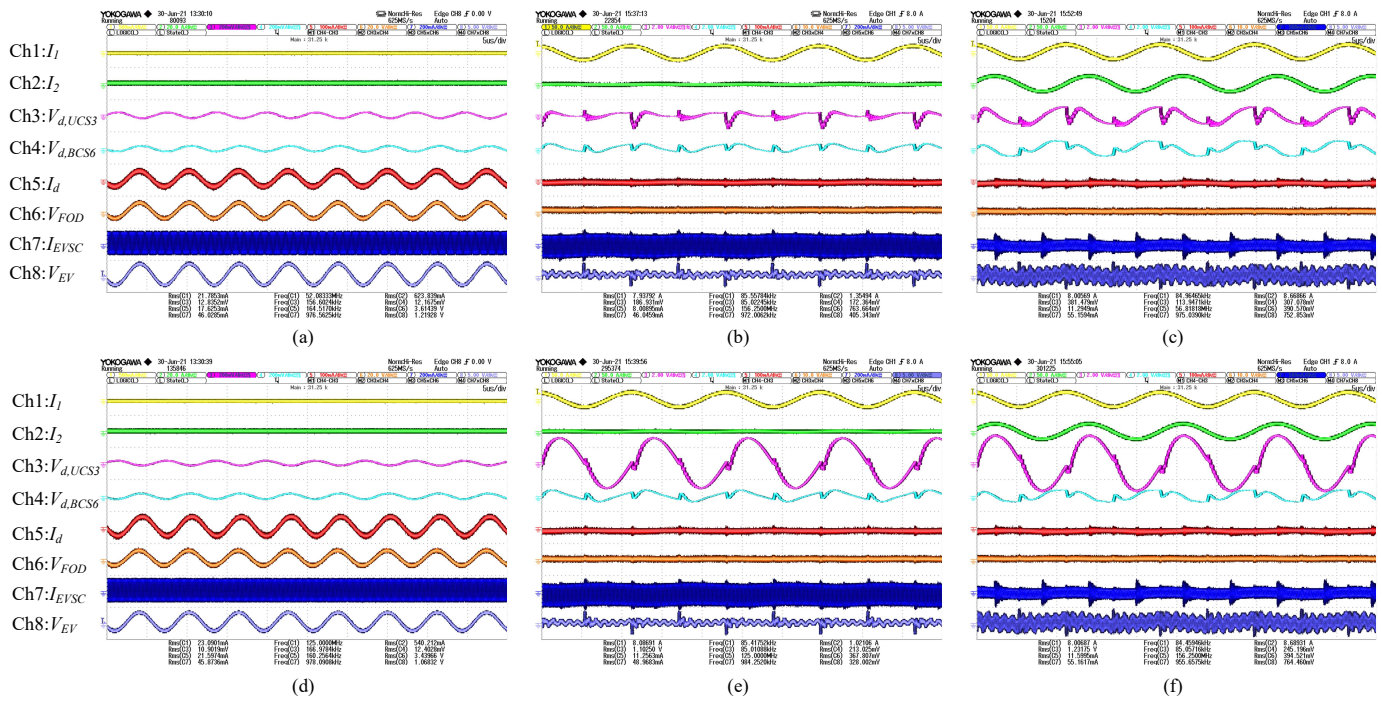


Fig. 23. System performances at different operating conditions. (a) the FOD-ACS operates with no MFOs and the Rx at p_{k-1} , (b) the FOD-PCS operates with the PS on, no MFOs and the Rx at p_{k-1} , (c) the EVD is triggered with the PS on, no MFOs and the Rx at p_k . (d) the FOD-ACS is triggered with a MFO on UCS-4 and the Rx at p_{k-1} , (e) the FOD-PCS is triggered with the PS on, a MFO on UCS-3 and the Rx at p_{k-1} . (f) the EVD triggered with the PS on, a MFO on UCS-3 and the Rx at p_k .

[15] J. Huh, S. W. Lee, W. Y. Lee, G. H. Cho, and C. T. Rim, "Narrow-Width Inductive Power Transfer System for Online Electrical Vehicles," *IEEE Transactions on Power Electronics*, vol. 26, no. 12, pp. 3666–3679, Dec. 2011.

[16] J. M. Miller, O. C. Onar, C. White, S. Campbell, C. Coomer, L. Seiber, R. Sepe, and A. Steyerl, "Demonstrating Dynamic Wireless Charging of an Electric Vehicle: The Benefit of Electrochemical Capacitor Smoothing," *IEEE Power Electronics Magazine*, vol. 1, no. 1, pp. 12–24, Mar. 2014.

[17] M. G. S. Pearce, G. A. Covic, and J. T. Boys, "Robust Ferrite-less Double D Topology for Roadway IPT Applications," *IEEE Transactions on Power Electronics*, pp. 1–1, 2018.

[18] B. Song, S. Dong, Y. Li, and S. Cui, "A Dual-Layer Receiver With a Low Aspect Ratio and a Reduced Output Fluctuation for EV Dynamic Wireless Charging," *IEEE Transactions on Power Electronics*, vol. 35, no. 10, pp. 10338–10351, Oct. 2020.

[19] B. Song, S. Cui, Y. Li, and C. Zhu, "A narrow-rail three-phase magnetic coupler with uniform output power for EV dynamic wireless charging," *IEEE Transactions on Industrial Electronics*, pp. 1–1, 2020.

[20] J. Shin, S. Shin, Y. Kim, S. Ahn, S. Lee, G. Jung, S. Jeon, and D. Cho, "Design and Implementation of Shaped Magnetic-Resonance-Based Wireless Power Transfer System for Roadway-Powered Moving Electric Vehicles," *IEEE Transactions on Industrial Electronics*, vol. 61, no. 3, pp. 1179–1192, Mar. 2014.

[21] D. Patil, M. K. McDonough, J. M. Miller, B. Fahimi, and P. T. Balsara, "Wireless Power Transfer for Vehicular Applications: Overview and Challenges," *IEEE Transactions on Transportation Electrification*, vol. 4, no. 1, pp. 3–37, Mar. 2018.

[22] F. Grazian, W. Shi, J. Dong, P. van Duijns, T. B. Soeiro, and P. Bauer, "Survey on Standards and Regulations for Wireless Charging of Electric Vehicles," in *2019 AEIT International Conference of Electrical and Electronic Technologies for Automotive (AEIT AUTOMOTIVE)*, Jul. 2019, pp. 1–5.

[23] K. Lee, Z. Pantic, and S. M. Lukic, "Reflexive Field Containment in Dynamic Inductive Power Transfer Systems," *IEEE Transactions on Power Electronics*, vol. 29, no. 9, pp. 4592–4602, Sep. 2014.

[24] Q. Deng, J. Liu, D. Czarkowski, M. Bojarski, J. Chen, W. Hu, and H. Zhou, "Edge Position Detection of On-line Charged Vehicles With Segmental Wireless Power Supply," *IEEE Transactions on Vehicular Technology*, vol. 66, no. 5, pp. 3610–3621, May 2017.

[25] A. N. Azad, A. Echols, V. A. Kulyukin, R. Zane, and Z. Pantic, "Analysis, Optimization, and Demonstration of a Vehicular Detection System Intended for Dynamic Wireless Charging Applications," *IEEE Transactions on Transportation Electrification*, vol. 5, no. 1, pp. 147–161, Mar. 2019.

[26] G. R. Nagendra, L. Chen, G. A. Covic, and J. T. Boys, "Detection of EVs on IPT Highways," *IEEE Journal of Emerging and Selected Topics in Power Electronics*, vol. 2, no. 3, pp. 584–597, Sep. 2014.

[27] A. Kamineni, M. J. Neath, A. Zaheer, G. A. Covic, and J. T. Boys, "Interoperable EV Detection for Dynamic Wireless Charging With Existing Hardware and Free Resonance," *IEEE Transactions on Transportation Electrification*, vol. 3, no. 2, pp. 370–379, Jun. 2017.

[28] Q. Wang, J. Zheng, B. Xu, and Y. Huang, "Analysis and experiments of vehicle detection with magnetic sensors in urban environments," in *2015 IEEE International Conference on Cyber Technology in Automation, Control, and Intelligent Systems (CYBER)*, Jun. 2015, pp. 71–75.

[29] R. M. Tyburski, "A review of road sensor technology for monitoring vehicle traffic," *ITE (Institute of Transportation Engineers) Journal (USA)*, vol. 59:8, Aug. 1988.

[30] Xiaoying Jin and C. H. Davis, "Vector-guided vehicle detection from high-resolution satellite imagery," in *IGARSS 2004. 2004 IEEE International Geoscience and Remote Sensing Symposium*, vol. 2, Sep. 2004, pp. 1095–1098.

[31] M. Rivas-López, C. A. Gomez-Sanchez, J. Rivera-Castillo, O. Sergiyenko, W. Flores-Fuentes, J. C. Rodríguez-Quinones, and P. Mayorga-Ortiz, "Vehicle detection using an infrared light emitter and a photodiode as visualization system," in *2015 IEEE 24th International Symposium on Industrial Electronics (ISIE)*, Jun. 2015, pp. 972–975.

[32] M. A. G. Clark, "Induction loop vehicle detector," US Patent US4 568 937A, Feb., 1986.

[33] W. Shi, F. Grazian, S. Bandyopadhyay, J. Dong, T. B. Soeiro, and P. Bauer, "Analysis of Dynamic Charging Performances of Optimized Inductive Power Transfer Couplers," in *2021 IEEE 19th International Power Electronics and Motion Control Conference (PEMC)*, Apr. 2021, pp. 751–756.

[34] S. Y. Jeong, V. X. Thai, J. H. Park, and C. T. Rim, "Self-Inductance-Based Metal Object Detection With Mistuned Resonant Circuits and Nullifying Induced Voltage for Wireless EV Chargers," *IEEE Transactions on Power Electronics*, vol. 34, no. 1, pp. 748–758, Jan. 2019.

[35] W. Shi, J. Dong, S. Bandyopadhyay, F. Grazian, T. B. Soeiro, and

- P. Bauer, "Comparative Study of Foreign Object and Misalignment in Inductive Power Transfer Systems," in *IECON 2019 - 45th Annual Conference of the IEEE Industrial Electronics Society*, vol. 1, Oct. 2019, pp. 2634–2639.
- [36] S. Fukuda, H. Nakano, Y. Murayama, T. Murakami, O. Kozakai, and K. Fujimaki, "A novel metal detector using the quality factor of the secondary coil for wireless power transfer systems," in *2012 IEEE MTT-S International Microwave Workshop Series on Innovative Wireless Power Transmission: Technologies, Systems, and Applications*, May 2012, pp. 241–244.
- [37] H. Kikuchi, "Metal-loop effects in wireless power transfer systems analyzed by simulation and theory," in *2013 IEEE Electrical Design of Advanced Packaging Systems Symposium (EDAPS)*, Dec. 2013, pp. 201–204.
- [38] M. Moghaddami and A. I. Sarwat, "A Sensorless Conductive Foreign Object Detection for Inductive Electric Vehicle Charging Systems Based on Resonance Frequency Deviation," in *2018 IEEE Industry Applications Society Annual Meeting (IAS)*, Sep. 2018, pp. 1–6.
- [39] N. Kuyvenhoven, C. Dean, J. Melton, J. Schwannecke, and A. E. Umenei, "Development of a foreign object detection and analysis method for wireless power systems," in *2011 IEEE Symposium on Product Compliance Engineering Proceedings*, Oct. 2011, pp. 1–6.
- [40] S. Y. Jeong, H. G. Kwak, G. C. Jang, S. Y. Choi, and C. T. Rim, "Dual-Purpose Nonoverlapping Coil Sets as Metal Object and Vehicle Position Detections for Wireless Stationary EV Chargers," *IEEE Transactions on Power Electronics*, vol. 33, no. 9, pp. 7387–7397, Sep. 2018.
- [41] V. X. Thai, G. C. Jang, S. Y. Jeong, J. H. Park, Y.-S. Kim, and C. T. Rim, "Symmetric Sensing Coil Design for the Blind-zone Free Metal Object Detection of a Stationary Wireless Electric Vehicles Charger," *IEEE Transactions on Power Electronics*, pp. 1–1, 2019.
- [42] L. Xiang, Z. Zhu, J. Tian, and Y. Tian, "Foreign Object Detection in a Wireless Power Transfer System Using Symmetrical Coil Sets," *IEEE Access*, vol. 7, pp. 44 622–44 631, 2019.
- [43] S. Verghese, M. P. Kesler, K. L. Hall, and H. T. Lou, "Foreign object detection in wireless energy transfer systems," US Patent US9442 172B2, Sep., 2016.
- [44] M. Budhia, J. T. Boys, G. A. Covic, and C. Huang, "Development of a Single-Sided Flux Magnetic Coupler for Electric Vehicle IPT Charging Systems," *IEEE Transactions on Industrial Electronics*, vol. 60, no. 1, pp. 318–328, Jan. 2013.
- [45] W. Shi, F. Grazian, J. Dong, T. B. Soeiro, and P. Bauer, "Detection of Metallic Foreign Objects and Electric Vehicles Using Auxiliary Coil Sets for Dynamic Inductive Power Transfer Systems," in *2020 IEEE 29th International Symposium on Industrial Electronics (ISIE)*, Jun. 2020, pp. 1599–1604.



Wenli Shi received the B.S. degree in automotive engineering from Jilin University, China, in 2015, and the M.S. degree in mechanical engineering from Beijing Insititue of Technology, China, in 2018. He is currently working towards the Ph.D. degree in the field of dynamic wireless charging of electric vehicles at the DC System, Energy Conversion and Storage (DCE&S) group, Delft University of Technology (TU Delft), The Netherlands. His research interests include foreign object detection, multi-objectives optimization design, dynamic modeling

and control for wireless power transfer.



Jianning Dong received his B.S. and Ph.D. degrees in electrical engineering from Southeast University, Nanjing, China, in 2010 and 2015, respectively. Since 2016, he has been an Assistant Professor at the DC System, Energy Conversion and Storage (DCE&S) group, Delft University of Technology (TU Delft), Delft, The Netherlands. Before joining TU Delft, he was a Postdoctoral Researcher at McMaster Automotive Resource Centre, McMaster University, Hamilton, ON, Canada. His research interests include electromechanical energy conversion

and contactless power transfer.



Thiago Batista Soeiro received the B.Sc. (Hons.) and M.Sc. degrees in electrical engineering from the Federal University of Santa Catarina, Florianopolis, Brazil, in 2004 and 2007, respectively, and the Ph.D. degree from the Swiss Federal Institute of Technology, Zurich, Switzerland, in 2012.

During the Master and Ph.D. studies, he was a visiting scholar at the Power Electronics and Energy Research Group, Concordia University, Montreal, QC, Canada, and at the Center for Power Electronics Systems, Blacksburg, VA, USA, respectively. From 2012 to 2013, he was a Researcher at the Power Electronics Institute, Federal University of Santa Catarina. From October 2013 to April 2018, he worked initially as a Scientist and later as a Senior Scientist at the Corporate Research Center, ABB Switzerland Ltd., Baden-Dattwil, Switzerland. Since May 2018, he has been working at the DC Systems, Energy Conversion and Storage Group, Delft University of Technology, Delft, The Netherlands. He is currently an Associate Professor and his research interests include advanced high power converters and dc system integration.

Dr. Soeiro was a recipient of the 2013 IEEE Industrial Electronics Society Best Conference Paper Award and the Best Paper Awards in the following IEEE conferences: International Conference on Power Electronics (ECCE Asia 2011), International Conference on Industrial Technology (ICIT 2013), Conference on Power Electronics and Applications EPE'15 (ECCE Europe 2015), and 19th International Power Electronics and Motion Control Conference (PEMC 2020).



Pavol Bauer received master's degree in electrical engineering from the Technical University of Kosice, Kosice, Slovakia, in 1985 and the Ph.D. degree from the Delft University of Technology, Delft, The Netherlands, in 1995.

He is currently a full Professor with the Department of Electrical Sustainable Energy of Delft University of Technology and head of DC Systems, Energy Conversion and Storage group. He received Masters in Electrical Engineering at the Technical University of Kosice ('85), Ph.D. from Delft University of Technology ('95) and title prof. from the president of Czech Republic at the Brno University of Technology (2008) and Delft University of Technology (2016). He is also honorary professor at Politehnica University Timisoira in Romania. From 2002 to 2003 he was working partially at KEMA (DNV GL, Arnhem) on different projects related to power electronics applications in power systems. He published over 95 journal and 350 conference papers in his field (with H factor Google scholar 39, Web of Science 29), he is an author or co-author of 8 books, holds 9 international patents and organized several tutorials at the international conferences. He has worked on many projects for industry concerning wind and wave energy, power electronic applications for power systems such as Smarttrafo; HVDC systems, projects for smart cities such as PV charging of electric vehicles, PV and storage integration, contactless charging; and he participated in several Leonardo da Vinci, H2020 and Electric Mobility Europe EU projects as project partner (ELINA, INETELE, E-Pragmatic, Micact, Trolley 2.0, OSCD) and coordinator (PEMCWebLab.com-Edipe, SustEner, Eranet DCMICRO). He is a Senior Member of the IEEE ('97), former chairman of Benelux IEEE Joint Industry Applications Society, Power Electronics and Power Engineering Society chapter, chairman of the Power Electronics and Motion Control (PEMC) council, member of the Executive Committee of European Power Electronics Association (EPE) and also member of international steering committee at numerous conferences.